

Gravity-Capillary Wave Spectral Modulation by Gravity Waves

Nathan J. M. Laxague, *Member, IEEE*, Milan Curcic, Jan-Victor Björkqvist, and Brian K. Haus, *Member, IEEE*

Abstract—In order to more fully understand the specific hydrodynamic relationship between young wind-generated gravity-capillary waves and longer gravity waves, a laboratory experiment was devised to observe changes in short wave spectral behavior over the phase of a long wave. This paper endeavors to expand on the body of laboratory wave modulation data and extend the investigation in support of the radar remote sensing of ocean surface waves. Measurements were made in the University of Miami’s surge-structure-atmosphere interaction facility in the air-sea interaction saltwater tank wind-wave tank, with 10 m referenced wind speeds ranging between 5 and 23 m/s and paddle-generated wave steepnesses “ak” varying between $0.05 < ak < 0.3$. A polarimetric camera was used to capture high sampling frequency maps of wave slope, yielding spatiotemporal information about short wind-wave behavior [provided as temporal variations in the wavenumber spectrum, where $k \approx \mathcal{O}(100-1000)$ rad/m]. The simultaneous and colocated long wave phase was measured via a side-looking camera. Hydrodynamic modulation transfer function (MTF) phases are found to be in general agreement with established values (between 2 and 10 radians) at the given wind speeds. The positive phase of the modulation places it immediately downwind of the long wave crest, with MTF magnitudes strongest for high wavenumbers at the lowest wind speeds. The results are also presented to show the modulation of gravity-capillary and pure capillary waves as variations in mean square slope over the long wave phase, with peak roughness enhancement found to move upwind of the long wave crest with increasing wind forcing.

Index Terms—Remote sensing, surface waves.

I. INTRODUCTION

THE interaction between long gravity waves and shorter wind-generated gravity-capillary waves has been the focus of inquiry in the wave and remote sensing research communities for some time. The presence of long waves has been found to change the growth and development of wind waves, altering the way in which momentum is transferred across the air-sea interface [6], [21]. Furthermore, the radar remote sensing of swell is made possible due to the periodic

Manuscript received October 27, 2016; revised December 9, 2016; accepted December 21, 2016. This work was supported in part by the Gulf of Mexico Research Initiative under Grant SA1207GOMRI005 and in part by the Office of Naval Research under Grant N000141410644. (*Corresponding author:* Nathan J. M. Laxague.)

N. J. M. Laxague, M. Curcic, and B. K. Haus are with the Rosenstiel School of Marine and Atmospheric Science, University of Miami, Miami, FL 33149 USA (e-mail: nlaxague@rsmas.miami.edu).

J.-V. Björkqvist is with the Finnish Meteorological Institute, Helsinki FI-00101, Finland.

Color versions of one or more of the figures in this paper are available online at <http://ieeexplore.ieee.org>.

Digital Object Identifier 10.1109/TGRS.2016.2645539

steepening and shallowing of Bragg scatterers orders of magnitude smaller than the swell itself [20].

The modulation transfer function (MTF) is an informative tool used in the investigation of this process. Though originally developed from microwave radar backscatter patterns [7], [16], advancements in short-scale wave measurement technologies have allowed the MTF to be computed directly through the observed hydrodynamic behavior of the ocean surface [5]. The complex-valued MTF contains within it information about the magnitude of long wave–short wave interaction and the long wave phase at which modulation occurs most strongly. Knowledge of this function’s dependence on atmospheric and sea-state conditions allows one a lens through which to interpret radar backscatter, improving the remote determination of those conditions.

Early studies of the interactions between long and short waves indicated that the greatest short-scale roughness enhancement occurs between the long wave’s crest and leading face [17], [21]. These studies made use of the optical properties of the air-sea interface to deduce long waves’ periodic variation of short wind-wave statistics. Later studies of similar technique found the magnification of short wave slope variance to trail the wave crest [5], [13]. Additional field efforts involving both radar backscatter [3], [15] and the short-scale slope fields as observed via scanning laser slope gauge [4] found a mixture of the aforementioned results, namely, that short-scale roughness enhancement tends to lead long wave crests in low wind speed and trail them in high wind speed. It was hypothesized that, for increasing wind forcing, hydrodynamic modulation of short waves due to velocity convergence becomes dominated by long wave modulation of the wind stress.

Fairly recently, numerical simulations [14] and laboratory experiments [2] found MTF magnitudes commensurate with previous studies and positive MTF phases that increased with increasing wind speed. However, there remains a lack of clarity regarding the nature of modulation that occurs away from the peak MTF phase. That is, a characterization of short wave behavior over the entire long wave. In past research, peak modulation was found to move upwind with increasing wind forcing. The purpose of this paper is to follow up on this and other findings, investigating the effect of long waves on short wave spectra in a both a time-averaged and a dynamic phase-resolving sense. This will place modern measurements of short wave modulation in an organic framework that accommodates hydrodynamic theory and the perspective gained from years of observations in this field.

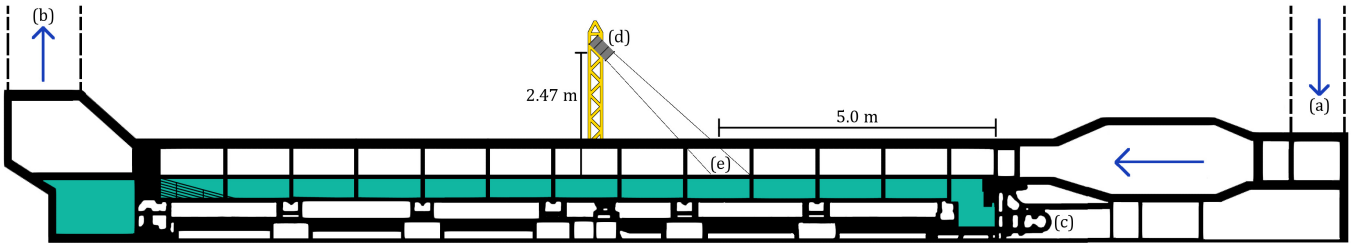


Fig. 1. Pictorial representation of ASIST wind-wave tank. (a) Wind inflow. (b) Wind outflow. (c) Hydraulic wavemaker. (d) Polarimetric camera. (e) Measurement location on water surface.

TABLE I
EXPERIMENTAL CONDITIONS

Paddle #	U_{10} [m/s]	u_* [m/s]	$\frac{c_p}{u_*}$ [rad]	Wave Steepness a_k [rad]
1	4.99	0.160	8.53	0.053
2	4.99	0.160	8.53	0.159
3	4.99	0.160	8.53	0.208
4	4.99	0.160	8.53	0.233
1	8.17	0.283	4.84	0.086
2	8.17	0.283	4.84	0.106
3	8.17	0.283	4.84	0.198
4	8.17	0.283	4.84	0.257
1	11.56	0.429	3.19	0.101
2	11.56	0.429	3.19	0.194
3	11.56	0.429	3.19	0.230
4	11.56	0.429	3.19	0.275
1	15.15	0.599	2.28	0.141
2	15.15	0.599	2.28	0.166
3	15.15	0.599	2.28	0.227
4	15.15	0.599	2.28	0.287
1	18.96	0.794	1.72	0.139
2	18.96	0.794	1.72	0.189
3	18.96	0.794	1.72	0.248
4	18.96	0.794	1.72	0.304
1	23.02	1.016	1.35	0.176
2	23.02	1.016	1.35	0.209
3	23.02	1.016	1.35	0.289
4	23.02	1.016	1.35	0.332

II. OBSERVATIONAL METHODS AND LABORATORY SETUP

The measurements used in this paper were performed at the University of Miami's surge–structure–atmosphere interaction facility in the air–sea interaction saltwater tank wind-wave tank (Fig. 1). The test section of the acrylic tank extends 15 m, with a $1 \text{ m} \times 1 \text{ m}$ cross-sectional area, and was filled with fresh water to a depth of 0.43 m. Measurements of water surface elevation and short wave shape were made over 24 trials of six wind speeds ($5 \text{ m/s} < U_{10} < 23 \text{ m/s}$) and four paddle-generated wave conditions with steepnesses ($0.05 < a_k < 0.3$), with six more in the absence of paddle waves. These values are shown Table I. Wind speed was measured via sonic anemometer, the sampling volume of which was centered at 0.285 m above the mean water level. The observed speeds were referenced to 10-m neutral values [19] in order to compare the results presented here with past results with greater ease. For all measurements, a current of 0.12 m/s was pumped through the sample volume in the wind and

wave direction. This mitigated the effects of surface wind and wave-induced currents returning along the bottom of the tank. Long wavenumber was fixed at 6.2 rad/m, producing an observed frequency of 1.35 Hz. This produced an essentially “deep water” wave, providing an opportunity to eliminate any potential variability that might be introduced from wave orbital motions that interact with the tank bottom. Furthermore, it has been observed that wave steepness is the crucial parameter in wave modulation [13], allowing us to study a range of modulation strengths merely by varying long wave amplitude.

In the remainder of this section, the optical methods utilized in the extraction of time-varying short wave slope fields and long wave elevation are explained. Furthermore, the fundamentals of the spectral analysis invoked in determination of short wave spectral behavior are elaborated.

A. Optical Determination of Long Wave Elevation

The instantaneous water surface elevation of the paddle-generated wave was determined via side-looking shadowgraph (Fig. 2). Long wave phase is described in MTF convention (Section II-D), with positive phase downwind of the long wave crest and negative phase upwind of the long wave crest. In this setup, a Basler Ace (piA1000-60 gm) camera was fitted with a 12-mm focal length lens (configured to minimize lens distortion) and oriented to face the side of the tank. The far side of the sampling volume was lit by an along-tank array of 1000-W halogen lamps in order to provide uniform illumination. The pixel resolution of this system was 0.0009 m/px, with 1000×1000 pixel frames acquired at 54 frames/s. The maximum of each frame’s intensity gradient was identified and interpreted as the air–sea interface. The use of this method allowed for a robust extraction of water surface elevation within the polarimetric camera frame. Cross-tank variations in paddle-generated long wave phase were not found to be of sufficient magnitude as to prohibit the use of shadowgraphy in the extraction of long wave water surface elevation.

B. Polarimetric Slope Sensing

Central to the analysis that follows is the extraction of the gravity-capillary wavenumber spectrum at a frequency sufficient to capture its behavior across many phases of a long wave. The polarimetric slope sensing (PSS) method [22]

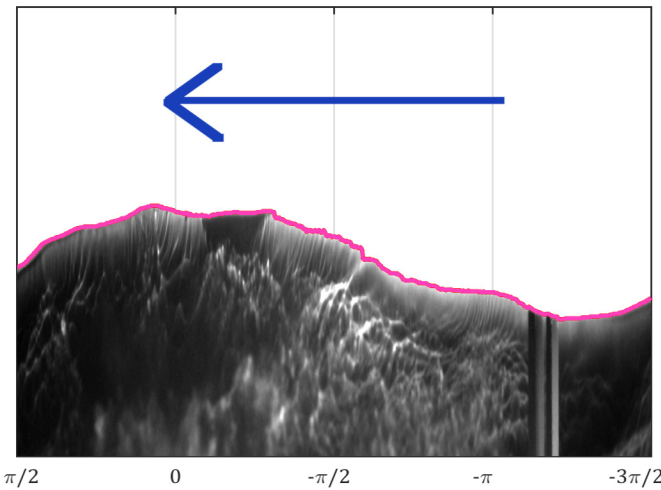


Fig. 2. Extraction of water surface elevation from shadowgraph images. Magenta line overlaid on grayscale image shows detection of water surface elevation. The wave is propagating from right to left as shown by the blue arrow, and the phase values are given along the horizontal axis. Long wave phase is described in MTF convention (Section II-D), with positive phase downwind of the long wave crest and negative phase upwind of the long wave crest. The water-side artifact in between $-\pi$ and $-3\pi/2$ is a spine in the acrylic, which did not affect the elevation measurements used here.

allows one to infer the 2-D slope field $\mathcal{S}(x, y)$ from its effect on the polarization of light reflected from the air-sea interface. For the setup used in this paper, a polarimeter [Fig. 3(a)] acquiring frames at 54 frames/s was positioned 2.47 m above the tank's mean water level and oriented at a 45° incidence angle. The imaged area of the water surface spanned $0.86 \text{ m} \times 0.86 \text{ m}$ [Fig. 3(b)], with a minimally resolvable wavelength of $\approx 2.26 \text{ mm}$ (Nyquist wavenumber of $\approx 2800 \text{ rad/m}$). The primary simplifying assumptions for this paper are that the incident light is unpolarized and the subsurface upwelling light may be neglected. A series of LEDs was used to supply an unpolarized light source, and black rubber lined the tank bottom to prevent spurious tank bottom reflections from influencing the slope field estimation. For these calculations, it was necessary to compute the Stokes parameters from the light intensities at 0° , 45° , and 90° linear polarization

$$\begin{aligned} S_0 &= I_0 + I_{90} \\ S_1 &= I_0 - I_{90} \\ S_2 &= 2 \cdot I_{45} - S_0. \end{aligned} \quad (1)$$

The Stokes parameters S_1 and S_2 are directly converted into the polarization orientation, from which follows the angle of intersection between the reflection and image planes. The tangent of this angle yields the wave slope in the cross-look direction

$$\phi = \frac{1}{2} \left[\pi + \tan^{-1} \left(\frac{S_2}{S_1} \right) \right] \quad \mathcal{S}_y = \tan(\phi). \quad (2)$$

In order to compute the wave slope in the along-look (here, along-tank) direction, the degree of linear polarization (DOLP)

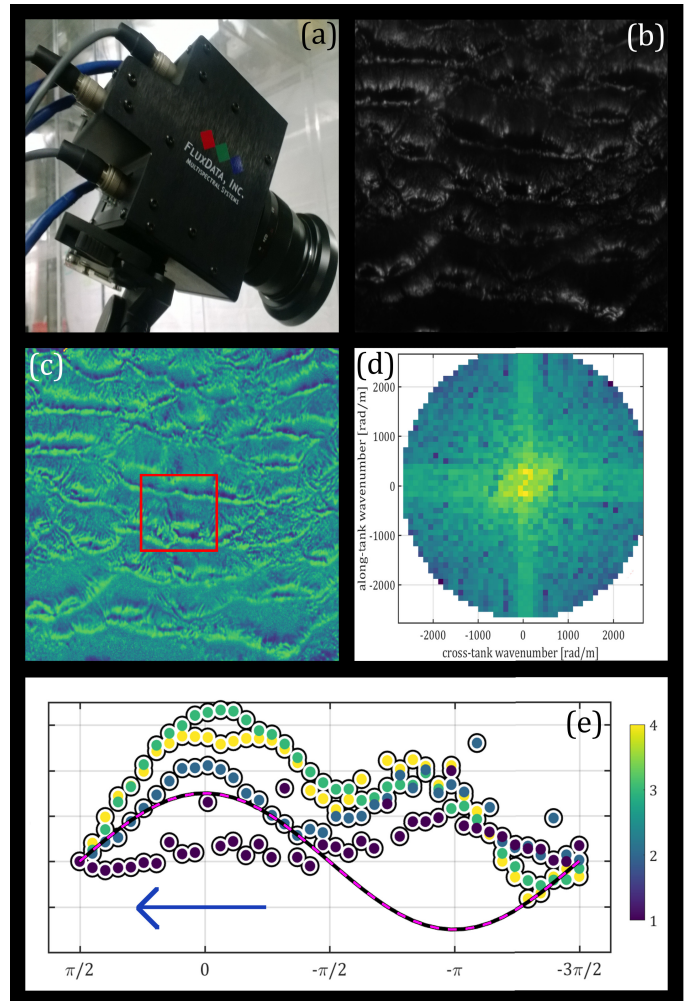


Fig. 3. Visualizations of outputs from PSS and associated spectral analysis. (a) Polarimetric camera enclosure. (b) 90° intensity image from camera. (c) Along-tank slope field corresponding to the same time step. (d) 2-D wavenumber slope spectrum, computed from a single snapshot's worth of data. (e) Mean square slope integrated from the spectrum computed in (d), plotted along the phase of a single long wave period. The blue arrow in (e) indicates the long wave propagation direction. Colors represent paddle conditions 1–4 as defined in Table I. The red box in (c) indicates the position of the slope field subwindow, and the red concentric circles in (d) mark out the corresponding regime in the short wave spectrum.

is generated using all three Stokes parameters

$$DOLP = \sqrt{\frac{S_1^2 + S_2^2}{S_0^2}} = \frac{r_\parallel^2 - r_\perp^2}{r_\parallel^2 + r_\perp^2} \quad (3)$$

$$r_\parallel = \frac{\tan(\theta_i - \theta_t)}{\tan(\theta_i + \theta_t)} \quad r_\perp = \frac{\sin(\theta_i - \theta_t)}{\sin(\theta_i + \theta_t)}. \quad (4)$$

Representing the DOLP in terms of the Fresnel reflection coefficients [(3); defined in (4)] enables one to extract the incidence angle of the reflected light. The variables θ_i and θ_t represent the angles made by incident and transmitted light with respect to the surface normal, respectively. Given knowledge of the index of refraction n and a diffuse lighting scheme, this allows one to directly compute the along-look slope of the reflecting surface [Fig. 3(c)]. For this analysis, n was taken to

be 1.33 based on the fresh water temperature of 20° C [12]

$$\theta_i = n \sin(\theta_t) \quad \mathcal{S}_x = \tan(\theta_i). \quad (5)$$

C. Short Wave Spectral Analysis

It is convenient to decompose the polarimeter-sensed wave slope fields produced in Section II-B into their constituent elements via Fourier analysis [10], [11]. For the purpose of evaluating short wave spectral properties at different long wave phases, a 50 × 50 pixel (5.5 cm × 5.5 cm) subsection was taken from the center of each rectified short wave slope field [Fig. 3(c)]. This was matched with the corresponding snippet from the shadowgraphy long wave elevation measurement [Fig. 3(e)]. The 5.5-cm subsection (approximately 20° of long wave phase) was chosen as to include a number of data points sufficient for the computation of a robust spectrum while remaining small enough to encapsulate a locally stationary segment of long wave slope. Once each slope field [that is, arrays of slope components $\mathcal{S}_x(x, y)$ and $\mathcal{S}_y(x, y)$ defined at each location (x, y) on the free surface $\eta(x, y)$] was trimmed to the appropriate region, it was subjected to a 2-D Fourier transform, yielding a 2-D slope spectrum $P(k_x, k_y)$ [Fig. 3(d)] with dimensions of meters squared; this spectrum is defined on the wavenumber interval [115, 2700 rad/m]

$$\begin{aligned} g_x(k_x, k_y) &= \int_0^Y \int_0^X e^{i(k_x x + k_y y)} \mathcal{S}_x(x, y) dx dy \\ g_y(k_x, k_y) &= \int_0^Y \int_0^X e^{i(k_x x + k_y y)} \mathcal{S}_y(x, y) dx dy. \end{aligned} \quad (6)$$

In this description, $x(k_x)$ and $y(k_y)$ represent displacement (magnitude in wavenumber space) and X and Y are the corresponding length and width of the imaged area on the water surface. One may compute the 2-D wavenumber slope spectrum $P(k_x, k_y)$ (dimensions of square meters) by multiplying the transformed function's magnitude by the appropriate constants

$$P(k_x, k_y) = \frac{|g_x|^2 + |g_y|^2}{Nk_{\max}^2} \quad (7)$$

where N is the number of data points, δ represents the camera's spatial resolution in meters per pixel, and $k_{\max} = (\pi)/(\delta)$. This spectrum may be integrated further with respect to azimuth angle φ in order to recover the omnidirectional wavenumber slope spectrum (note the Jacobian k in the integrand)

$$P(k) = \int_0^{2\pi} k P(k, \varphi) d\varphi \quad (8)$$

where $k = (k_x^2 + k_y^2)^{1/2}$ and $P(k)$ is the omnidirectional slope spectrum. $P(k)$ is alternatively equivalent to $k^2 \Psi(k)$, where $\Psi(k)$ is the omnidirectional elevation spectrum. In addition, $P(k) = k^{-1} B(k)$, where $B(k)$ is the omnidirectional dimensionless saturation spectrum. Mean square slope $\langle \mathcal{S}^2 \rangle$ (hereafter referred to as \mathcal{R} for simplicity) is the zeroth moment of the omnidirectional slope spectrum $P(k)$ (9); this quantity will be computed over several wavenumber ranges

TABLE II
WAVENUMBER RANGE CLASSIFICATION

Wavenumber Range	Classification
112.7 rad/m < k < 371 rad/m	Gravity-capillary regime, part one
371 rad/m < k < 1173 rad/m	Gravity-capillary regime, part two
1173 rad/m < k	Capillary regime

(Table II) for the purpose of investigating multiscale roughness variability

$$\mathcal{R}_{ij} = \int_{k_i}^{k_j} P(k) dk. \quad (9)$$

The so-called tilt modulation has not been mentioned thus far. It is a component of the observed backscattered power modulation that is well known in the radar remote sensing community. This contribution arises from periodic changes in the orientation of Bragg scatterers relative to the observer and is not reflective of fluid modulation that exists irrespective of reference frame. While Bragg scattering does not play a part in the PSS method, a potential bias that presents similarly to tilt modulation may arise due to inadequate frame rectification onto the wavy surface. The subwindow used to calculate the parameters extracted in this paper has been assumed to be a square resting at the mean water level. Of course, the very nature of the study violates this assumption, with the patch on the water surface taking the form of a slightly bent trapezoid that changes in shape as a function of the long wave phase. However, the maximum angle that this patch takes relative to the mean water level (for paddle case #4 at the highest wind speed) results only in a ≈5.4% variation in the along-tank scale. When considering the effect of this bias on the wavenumber spectrum, the slope spectral density varies ≈0.3% from its assumed value at the phase of maximum distortion, corresponding to a share of less than 1% of the total observed short wave modulation. In summary, even though these perspective-based oscillations in subwindow scale are coherent with the modulation that has been hypothesized and observed here, they represent a negligible piece of the overall variation and therefore do not confound the results.

D. Computing the Modulation Transfer Function

The hydrodynamic modulation of short waves by long waves is typically quantified by the MTF [7], [16]. The analysis that follows focuses on the modulation of particular wavenumber bands of the short wave mean square slope \mathcal{R} . The MTF is therefore presented as a normalized form of the cross spectrum $C_{\mathcal{R}\eta}(f)$ between $\mathcal{R}(t)$ and $\eta(t)$ [4]

$$\mathcal{M}(f) = \frac{1}{k' \langle \mathcal{R} \rangle} \frac{C_{\mathcal{R}\eta}(f_0)}{C_{\eta\eta}(f_0)} \quad (10)$$

where f_0 is the observed gravity wave frequency and f is the intrinsic gravity wave frequency. $C_{\eta\eta}(f)$ is the autospectrum of the gravity wave elevation, $\langle \mathcal{R} \rangle$ is the time average of the mean square slope, and k' is the deep water gravity wavenumber from linear wave theory given the intrinsic frequency f

$$k' = (2\pi f)^2 g^{-1} \quad (11)$$

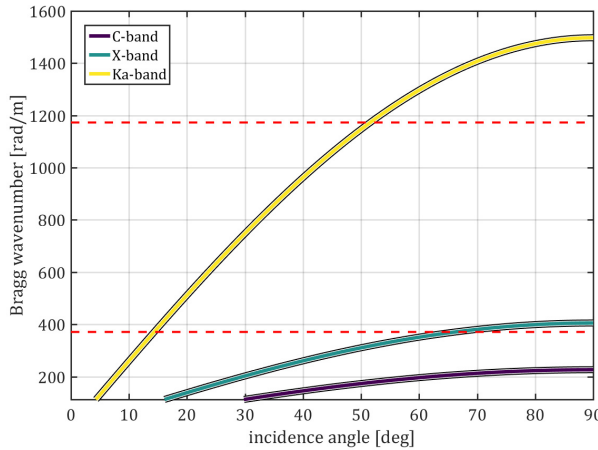


Fig. 4. Bragg wavenumbers for C-, X-, and Ka-bands as a function of incidence angle. Red dashed lines demarcate gravity-capillary regime #1 ($112.7 < k < 371$ rad/m), gravity-capillary regime #2 ($371 < k < 1173$ rad/m), and the capillary regime (1173 rad/m $< k$) following Table II.

with g the acceleration due to gravity (9.81 m/s 2). The computed MTF $\mathcal{M}(f)$ is a complex quantity—its magnitude describes the strength of the modulation and its phase describes the lag or lead of the modulation with respect to the long wave crest. For the MTF formulation given in (10), a positive phase indicates that peak modulation leads (occurs downwind of) the long wave crest, while a negative phase indicates that peak modulation lags (occurs upwind of) the long wave crest.

Rather than computing the MTF for the mean square slope as split into wavenumber ranges of arbitrary size and location, we have partitioned the mean square slope into three subdivisions, given in Table II [10] and shown in Fig. 4. Each corresponds to a different regime of the deep water gravity-capillary linear dispersion relation (12) given $g = 9.81$ m/s 2 , $\sigma = 0.072$ N/m, and $\rho = 998.2$ kg/m 3

$$\omega^2 = gk + \frac{\sigma}{\rho}k^3. \quad (12)$$

For gravity-capillary regime #1, the “gravity” term gk is greater than, but of the same order as, the “capillary” term $\sigma/\rho k^3$. For gravity-capillary regime #2, gk is less than, but of the same order as, $\sigma/\rho k^3$. For the capillary regime, $\sigma/\rho k^3$ is at least an order of magnitude greater than gk .

III. RESULTS

In this section, the aforementioned methods are applied to the laboratory study of hydrodynamic modulation of short waves by long waves. The sensitivity of short wave spectra to long wave steepness and wind speed is described. Phase-preserving “ensembles” in which the short-scale roughness of many long wave periods is averaged allow for the examination of short wave characteristics as a function of long wave phase. Mean square slope MTFs are computed for particular wavenumber regimes, allowing for the interpretation of MTF outputs in both a physical restoring force frame of reference and a radar remote sensing band frame of reference (i.e., as in Fig. 4).

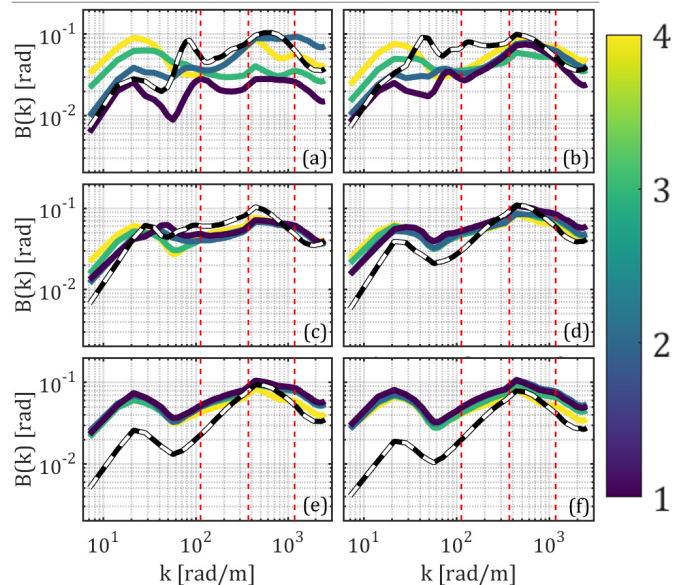


Fig. 5. Saturation spectrum $B(k)$ [rad] for all six wind speed conditions. (a) 4.99 m/s. (b) 8.17 m/s. (c) 11.56 m/s. (d) 15.15 m/s. (e) 18.96 m/s. (f) 23.02 m/s. Colors correspond to the paddle numbers as listed in Table I. Black and white dashed lines indicate spectral density in the absence of paddle waves. Red dashed lines mark the regimes defined in Table II

A. Time-Averaged Dependence of Short Wave Spectra on Long Waves and Wind Speed

Fig. 5 shows the time-averaged short wave spectra computed over the full slope field. For low wind speeds, the presence of paddle waves actually results in the reduction of spectral energy density at moderate [$\mathcal{O}(100)$ rad/m] wavenumbers. Note that, for low wavenumbers ($k < 20$ rad/m), spectral energy density does not increase as it should with the imposition of a $k = 6.2$ -rad/m long wave. This is an artifact of the poor resolution of those waves in the 0.86 m \times 0.86 m sensing footprint; however, this gap in resolution does not appreciably affect any single portion of the following analysis due to the fact that these waves are observed via shadowgraphy. Ultimately, their gap in the polarimetric spectra has a negligible effect on the short-scale wave analysis that forms the greatest share of this research. In a manner similar to Fig. 5, Fig. 6 shows the average impact of long waves on short-scale roughness. For $U_{10} < 18$ m/s, the presence of long waves is found to reduce the time-averaged mean square slope for all but the highest paddle wave steepness. This effect weakens (i.e., roughness is enhanced) with increases in long wave steepness and wind forcing magnitude. This is very likely due to the waves’ alteration of the manner in which momentum is transferred from the wind to the water—the dominant gravity waves are taking the momentum that might otherwise generate gravity-capillary waves [21]. This interpretation is supported by the fact that wave steepness (that is, dominant wave amplitude) is shown to increase with increasing wind speed magnitude (Table I). Only for the high wind cases ($U_{10} > 18$ m/s), does the presence of long waves enhance the observed surface roughness for all wave steepnesses. The roughness enhancement ceases to show sensitivity to long

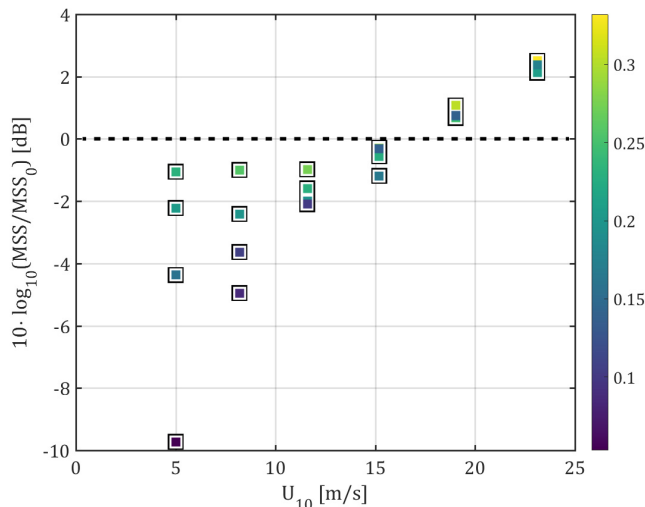


Fig. 6. Mean square slope for wind plus paddle conditions relative to wind-only condition (MSS_0), given in decibels as a function of U_{10} . Colorbar indicates long wave steepness α_k in radians. The horizontal dashed line indicates 0 dB, separating mean square slope enhancement by long waves (top) from mean square slope reduction by long waves (bottom).

wave steepness in that regime, indicating the dominance of wind forcing over wave hydrodynamic effects (as in [4]).

B. Variations in Short Wave Spectral Energy Over Long Wave Phase

Fig. 9 shows the value of mean square slope \mathcal{R} relative to its phase = $\pi/2$ value (given in decibels). Fig. 9 is separated into the three short wave regimes described in Table II (top: gravity-capillary #1, middle: gravity-capillary #2, and bottom: capillary). Note that \mathcal{R} is shown relative to $\mathcal{R}(0)$, not the wind-only mean square slope as in Fig. 6. The phase-varying behavior in \mathcal{R} reduces dramatically for increasing wind speed [Fig. 9(a)–(f)] at the mild paddle wave conditions while persisting for the two steepest paddle conditions. This is most apparent for mean square slope computed over the capillary wave regime, with phase dependence vanishing for even moderate wind forcing. The maximum value of \mathcal{R} typically occurs at or around the long wave crest, with increases in short-scale roughness enhancement found to go from downwind of the crest [Fig. 9(a)] to upwind of the crest [Fig. 9(f)] with increasing wind speed. This result is similar to a result of past field observations in which peak modulation was found to progress upwind for increasing wind forcing [4].

C. Interpreting the Modulation Transfer Function

The MTFs computed for these mean square slope subdivisions are given in Fig. 7, presented alongside past results [3], [8], [18], with magnitude [Fig. 7(a), (c), and (e)] and phase [Fig. 7(b), (d), and (f)] shown as columns. The MTF magnitudes computed here for gravity-capillary regime #1 do not show a dependence on wind speed or paddle wave steepness. The magnitudes for gravity-capillary regime #2 and the capillary regime, however, exhibit considerable scatter with respect to long wave steepness at low wind speeds that quickly tamps down, settling below the gravity-capillary #1 MTF magnitudes.

Note the MTF magnitudes shown in Fig. 7(e) for the lowest wind speed cases; their greatly scattered high values mirror the observations of relative mean square slope (Fig. 6) for the same conditions. MTF phases are almost all positive, with the vast majority lying between 0° and 90° and centered around 45° on the leading face of the long wave. The few MTF phases to exceed 90° occur for low winds and slight paddle wave steepnesses. No appreciable difference in MTF phase exists across the three mean square slope subdivisions, suggesting that the position of peak modulation does not vary with short wave scale in the way that the magnitude of modulation does.

D. Going a Step Further: Visualizing Temporal Short Wave Evolution

Due to the fact that the PSS method is able to acquire wave spatial information at a high sampling rate, one may use it to sense nonstationary time-varying phenomena. Fig. 8 shows windsea's spectral response to the impingement of long paddle-generated waves, with Fig. 8(a)–(c) representing mean square slope \mathcal{R} relative to the wind-only case and computed over the wavenumber regimes gravity-capillary #1, gravity-capillary #2, and capillary, respectively. The lowest wind speed case ($U_{10} = 4.99$ m/s) was chosen in order to visually emphasize the role of wave steepness. Enhancement of short-scale roughness is found to occur on the leading face of the long wave immediately after its arrival into the sampling window. An amount of time shorter than a long wave period is needed for the gravity-capillary waves to settle into their steady behavior, an observation that fits with theory given the waves' relatively short [$\mathcal{O}(0.1)$ s] relaxation times [9]. In addition, the short wave spectral energy density is reduced for paddle condition #1 (violet line), especially for Fig. 8(c), the capillary regime.

IV. DISCUSSION

The presence of long paddle-generated waves is found to reduce average short wave spectral energy density at low wind speeds (Fig. 5). A consequence of this reduction is the diminishment of mean square slope (Fig. 6). This is a strong indicator that the long waves have altered the manner in which the short waves are receiving momentum from the wind forcing, in agreement with past results [2], [21]. Early laboratory measurements showed that the greatest increase in short wave slope variance occurs slightly downwind of the crest [17], [21], and more recent numerical studies have corroborated this result [14]. Furthermore, orbital velocity convergence on the leading face of the wave is hypothesized to enhance short wave dissipation [17].

The presence of pre-existing waves has been shown to reduce the atmospheric roughness length at low wind speeds [21]. Recent results from PIV analysis of air flow over long waves [1] have directly shown that streamlines do not detach from the gently sloping waves that make up the mildest case here. However, for long waves of moderate to high steepness [$\mathcal{O}(0.1)$ rad], flow separation from wave crests has been shown to occur, inducing turbulent fluctuations in the wind field. This transition presents a realistic explanation for the short wave behavior described here. All of the long

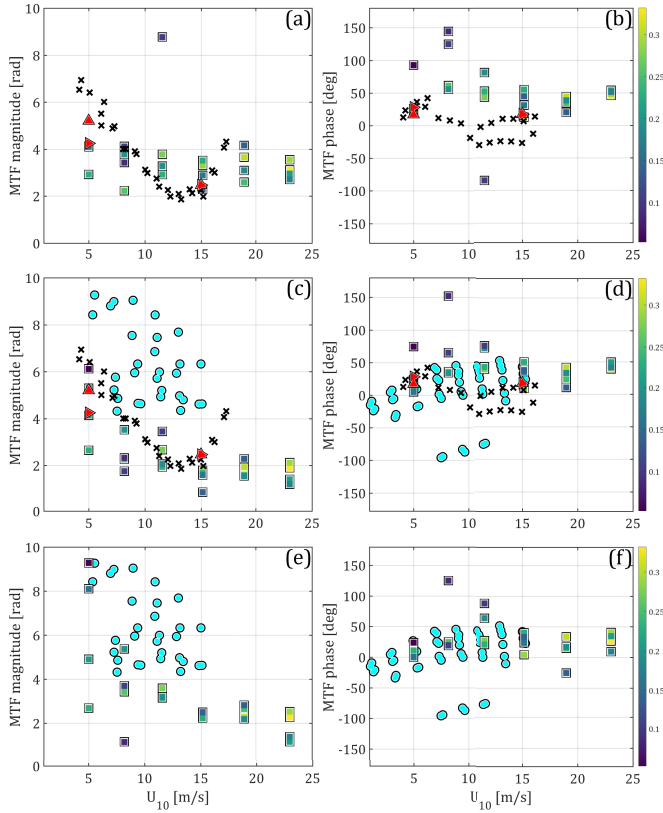


Fig. 7. Magnitude and phase of the mean square slope MTF as a function of U_{10} . (a) and (b) Gravity-capillary regime #1. (c) and (d) Gravity-capillary regime #2. (e) and (f) Capillary regime. Colorbar indicates long wave steepness α_k in radians. Red top and right-facing triangles show the three-phase model MTF results from [18] for X-band radar at HH and VV polarizations, respectively. Black x-marks represent observed MTFs computed from X-band radar data collected during MARSEN [3]. Cyan circles represent observed MTFs computed from Ka-band radar data collected during SAXON-FPN [8].

paddle-generated waves produced for this paper immediately become the dominant scale for momentum flux. For waves of low steepness, streamlines stay attached to the wavy interface and maintain a surface of relative aerodynamic smoothness. However, for increasingly steep long waves, flow separation induces increasingly energetic turbulent fluctuations, which in turn fuel the growth of gravity-capillary waves and partially offset the loss of atmospheric momentum to the dominant wave scale.

Past field measurements have indicated that, at low wind speeds, velocity convergence from long wave orbitals dominates the MTF, giving a phase > 0 . Conversely, it is indicated that at high wind speeds, wind stress modulation dominates the MTF, giving a phase < 0 [3], [4]. Although this transition is not recorded in the MTFs computed here, evidence of its occurrence can be found in Fig. 9, as the peak value of mean square slope enhancement creeps upwind from the leading face of the long wave with increasing wind speed. This apparent discrepancy likely arises due to the fact that the MTF locates peak modulation, while the modulation diagrams presented in Fig. 9 show roughness response across the entire long wave. Therefore, nondominant enhancement of mean square slope that occurs away from peak modulation in response to greater wind forcing will not change the MTF

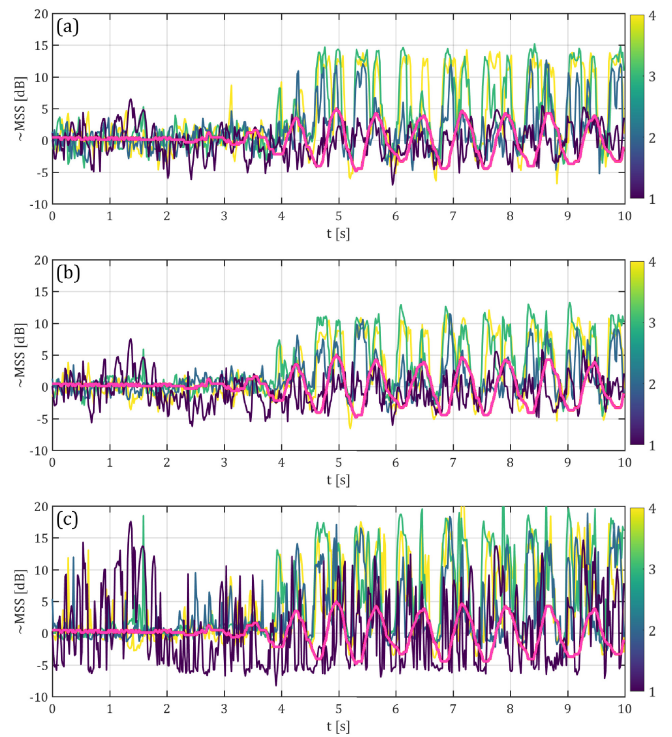


Fig. 8. Time series of relative mean square slope, partitioned into (a) gravity-capillary #1, (b) gravity-capillary #2, and (c) capillary. A representative time series of water surface elevation is overlaid on each panel as a guide. Wind speed $U_{10} = 4.99$ m/s for (a)–(c). Colors correspond to paddle conditions as described in Table I.

phase. The relatively high steepnesses of the paddle-generated waves given here lead to hydrodynamic dominance in the total modulation, supporting this interpretation.

Further insight into the laboratory-obtained MTFs may be gained via comparison with past remote sensing data. In order to perform this comparison, it is necessary to identify the remote sensing parameters that correspond to the wavenumber regimes noted in Table II. Fig. 4 shows the Bragg wavenumber as a function of incidence angle for C-band (here 5.5 cm), X-band (here 3.1 cm), and Ka-band (here 0.84 cm) systems. Evidently, for SAR and scatterometry at typical angles of incidence, C-band and X-band systems will sense in the “gravity-capillary #1” regime and Ka-band systems will sense in the “gravity-capillary #2” regime. The pure capillary regime will still be sensed by Ka-band sensors fixed at moderate to high incidence angles. With this information in mind, we use Fig. 7 to compare laboratory observations with field observations [marine remote sensing experiment (MARSEN) [3]; synthetic aperture radar and x-band ocean nonlinearities—Forschungsplattform Nordsee (SAXON-FPN) [8]] and the results of a three-phase model MTF [18], the latter of which shows especially good qualitative agreement with the results presented here. These laboratory-obtained MTFs and the field MTFs produced from data collected in the North Sea should not necessarily be expected to perfectly match due to the order of magnitude difference in long wave steepness. However, the fact that the MTF magnitudes obtained from Ka-band radar [8] are greater than the laboratory MTF magnitudes is consistent with what one might predict for modulation of

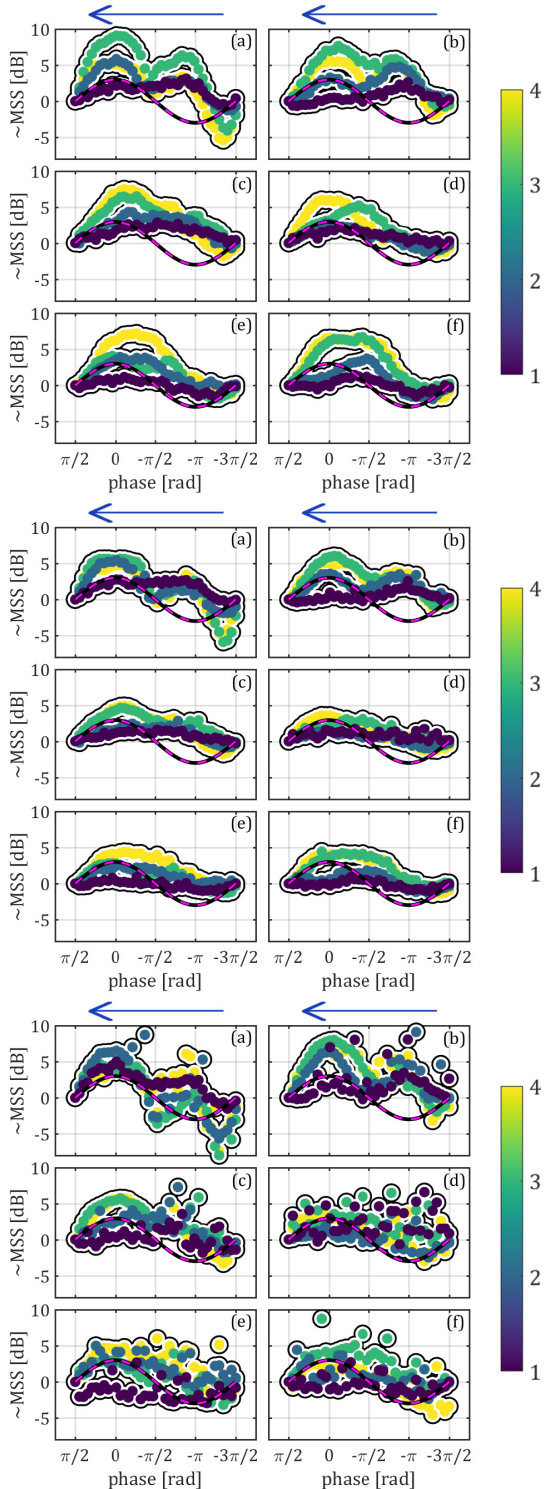


Fig. 9. Change in mean square slope given relative to each condition's value at phase = 0 and plotted as a function of long wave phase. Data are partitioned by short wave regime as in Table II (top: gravity-capillary #1, middle: gravity-capillary #2, and bottom: capillary). Subfigures correspond to the six wind speed conditions. (a) 4.99 m/s. (b) 8.17 m/s. (c) 11.56 m/s. (d) 15.15 m/s. (e) 18.96 m/s. (f) 23.02 m/s. Colors represent the paddle conditions as described in Table I. The magenta dashed line simulates the shape (arbitrary magnitude) of the long wave as a function of phase.

high wavenumber waves via long waves of low steepness. For all results, MTF magnitude is found to be greatest at low wind speed, dropping precipitously with increasing wind

speed. Greatest variability in MTF magnitude is also found to occur at low wind speeds, especially for Ka-band and pure capillary results. For the majority of transmission bands and polarizations, MTF phases are > 0 , downwind of crests between 20° and 60° .

V. CONCLUSION

The results presented here offer a strong confirmation of past results regarding modulation magnitude and phase, namely, that peak modulation leads the long wave crest [17], [21] and that wind forcing dominates hydrodynamic modulation at high (> 18 m/s) wind speeds [3], [4]. In addition, the phase-resolving roughness behavior summarized in Fig. 9 offers this paper's truly novel insight into short wave modulation. This view of short wave spectral response to each portion of the long wave extends beyond the traditional snippet view of the MTF, directly portraying the transition from hydrodynamic to aerodynamic modulation over the full long wavelength. The partitioning of the mean square slope into subdivisions has allowed us to investigate the short-scale wave response to modulation in connection to both physical restoring force (Table II) and the radar remote sensing bands that might observe each segment of roughness (Fig. 4). The partitioning of surface roughness by physical restoring force also allows one to see the critical susceptibility of the shortest waves to wind forcing modulation. The nonstationary case study shown in Fig. 8 adds to these results, showing the reduction in surface roughness for low steepness long waves and the dramatic phase-coherent enhancement for high steepness long waves. This effort directly unifies the scale-separated modulation information shown in Figs. 7 and 9 with past examples of comprehensive radar remote sensing analysis [8], [18], building on the connection between the direct observation of hydrodynamic wave modulation and radar remote sensing of ocean surface waves.

ACKNOWLEDGMENT

The authors would like to thank C. Guigand for the work, who provided valuable technical expertise and labor in arranging all portions of the data acquisition. The authors would also like to thank M. Rebozo, S. Mehta, and H. Dai for their help in setting up the wind-wave tank.

REFERENCES

- [1] M. P. Buckley and F. Veron, "Structure of the airflow above surface waves," *J. Phys. Oceanogr.*, vol. 46, no. 5, pp. 1377–1397, 2016.
- [2] M. A. Donelan, B. K. Haus, W. J. Plant, and O. Troianowski, "Modulation of short wind waves by long waves," *J. Geophys. Res. Oceans*, vol. 115, no. C10, pp. 1–12, 2010.
- [3] T. Hara and W. J. Plant, "Hydrodynamic modulation of short wind-wave spectra by long waves and its measurement using microwave backscatter," *J. Geophys. Res. Oceans*, vol. 99, no. C5, pp. 9767–9784, 1994.
- [4] T. Hara, K. A. Hanson, E. J. Bock, and B. M. Uz, "Observation of hydrodynamic modulation of gravity-capillary waves by dominant gravity waves," *J. Geophys. Res., Oceans*, vol. 108, no. C2, pp. 2156–2202, 2003, doi: 10.1029/2001JC001100.
- [5] P. A. Hwang, "Microstructure of ocean surface roughness: A study of spatial measurement and laboratory investigation of modulation analysis," *J. Atmos. Ocean. Technol.*, vol. 16, no. 11, pp. 1619–1629, 1999.

- [6] K. K. Kahma, M. A. Donelan, W. M. Drennan, and E. A. Terray, "Evidence of energy and momentum flux from swell to wind," *J. Phys. Oceanogr.*, 2016.
- [7] W. C. Keller and J. W. Wright, "Microwave scattering and the straining of wind-generated waves," *Radio Sci.*, vol. 10, no. 2, pp. 139–147, 1975.
- [8] W. C. Keller, W. J. Plant, R. A. Petitt, and E. A. Terray, "Microwave backscatter from the sea: Modulation of received power and Doppler bandwidth by long waves," *J. Geophys. Res. Oceans*, vol. 99, no. C5, pp. 9751–9766, 1994.
- [9] V. Kudryavtsev, D. Akimov, J. Johannessen, and B. Chapron, "On radar imaging of current features: 1. Model and comparison with observations," *J. Geophys. Res. Oceans*, vol. 110, no. C7, pp. 2156–2202, 2005, doi: 10.1029/2004JC002505.
- [10] N. J. M. Laxague, B. K. Haus, D. Bogucki, and T. Özgökmen, "Spectral characterization of fine-scale wind waves using shipboard optical polarimetry," *J. Geophys. Res. Oceans*, vol. 120, no. 4, pp. 3140–3156, 2015.
- [11] N. J. M. Laxague, D. G. Ortiz-Suslow, B. K. Haus, N. J. Williams, and H. C. Gruber, "Water surface slope spectra in nearshore and river mouth environments," in *Proc. IOP Conf. Ser. Earth Environ. Sci.*, 2016, vol. 35, no. 1, p. 012013.
- [12] R. C. Millard and G. Seaver, "An index of refraction algorithm for seawater over temperature, pressure, salinity, density, and wavelength," *Deep Sea Res. A. Oceanogr. Res. Papers*, vol. 37, no. 12, pp. 1909–1926, 1990.
- [13] S. J. Miller, O. H. Shemdin, and M. S. Longuet-Higgins, "Laboratory measurements of modulation of short-wave slopes by long surface waves," *J. Fluid Mech.*, vol. 233, pp. 389–404, Apr. 2006.
- [14] G. Pan and J. T. A. Johnson, "A numerical study of the modulation of short sea waves by longer waves," in *Proc. IEEE Int. Conf. Geosci. Remote Sens. Symp. (IGARSS)*, Sep. 2006, pp. 1304–1307.
- [15] W. J. Plant, "A two-scale model of short wind-generated waves and scatterometry," *J. Geophys. Res. Oceans*, vol. 91, no. C9, pp. 10735–10749, 1986.
- [16] W. J. Plant, "The modulation transfer function: Concept and applications," in *Radar Scattering From Modulated Wind Waves*. Bergen aan Zee, The Netherlands: Springer, 1989, pp. 155–172.
- [17] A. M. Reece, Jr., "Modulation of short waves by long waves," *Boundary-Layer Meteorol.*, vol. 13, nos. 1–4, pp. 203–214, 2015.
- [18] R. Romeiser, A. Schmidt, and W. A. Alpers, "A three-scale composite surface model for the ocean wave-radar modulation transfer function," *J. Geophys. Res. Oceans*, vol. 99, no. C5, pp. 9785–9801, 1994.
- [19] S. D. Smith, "Coefficients for sea surface wind stress, heat flux, and wind profiles as a function of wind speed and temperature," *J. Geophys. Res. Oceans*, vol. 93, no. C12, pp. 15467–15472, 1998.
- [20] J. W. Wright, "Detection of ocean waves by microwave radar; the modulation of short gravity-capillary waves," *Boundary-Layer Meteorol.*, vol. 13, nos. 1–4, pp. 87–105, 1978.
- [21] J. Wu, "Effects of long waves on wind boundary layer and on ripple slope statistics," *J. Geophys. Res.*, vol. 82, no. 9, pp. 1359–1362, 1997.
- [22] C. J. Zappa, M. L. Banner, H. Schultz, A. Corrada-Emmanuel, L. B. Wolff, and J. Yalcin, "Retrieval of short ocean wave slope using polarimetric imaging," *Meas. Sci. Technol.*, vol. 19, no. 13, pp. 1359–1362, 2008.



Nathan J. M. Laxague (M'16) received the B.S. degree in physics and the Ph.D. degree in applied marine physics from the University of Miami, Coral Gables, FL, USA, in 2011 and 2016, respectively.

He is currently a Postdoctoral Associate together with Dr. Brian Haus with the Department of Ocean Sciences, Alfred C. Glassell, Jr. SUSTAIN (SUrge-Structure-Atmosphere Interaction) Laboratory, Miami, FL, USA.



Milan Curcic received the B.Sc. degree in meteorology from the University of Belgrade, Belgrade, Serbia, in 2009, and the Ph.D. degree in meteorology and physical oceanography from the University of Miami, Coral Gables, FL, USA, in 2015.

He is currently a Postdoctoral Associate with Prof. S. Chen with the Department of Ocean Sciences, University of Miami.



Jan-Victor Björkqvist received the B.Sc. and M.Sc. degrees in mathematics from the University of Helsinki, Helsinki, Finland, in 2012. He is currently pursuing the Ph.D. degree in oceanography in the University's Doctoral Programme in atmospheric sciences.

He is currently a Research Scientist together with Dr. H. Pettersson with the Finnish Meteorological Institute, Helsinki.



Brian K. Haus (M'0) received the B.S. degree in ocean science, the M.S.E. degree, and the Ph.D. degree in coastal engineering from the University of Michigan, Ann Arbor, MI, USA, in 1987, 1989, and 1992, respectively.

He is currently a Professor with the Ocean Sciences Department, Rosenstiel School for Marine and Atmospheric Science, University of Miami, Miami, FL, USA. His research interests include the experimental studies of air-sea interactions, ocean surface currents, radar remote sensing of oceanographic processes, shelf and estuary dynamics, and wave-current interactions.